

Contents lists available at ScienceDirect

International Journal of Plasticity

journal homepage: www.elsevier.com/locate/ijplas





Modeling the non-Schmid crystallographic slip in MAX phases

Umair Bin Asim, Zhiqiang Zhan, Miladin Radovic, Ankit Srivastava

Department of Materials Science and Engineering, Texas A&M University, College Station, TX, USA

ARTICLE INFO

Keywords:
Constitutive behavior
Crystal Plasticity
Layered material
Non-Schmid effect
Finite elements

ABSTRACT

We present a crystal plasticity constitutive relation for the description of experimentally observed non-Schmid crystallographic slip in a class of ternary carbides and nitrides commonly referred to as MAX phases. In the constitutive relation, we assume that the evolution of the slip system strength in MAX phases has two components – a classical component that depends on the Taylor cumulative shear strain and a non-Schmid component that depends on the stress normal to the slip plane. The non-Schmid crystal plasticity constitutive relation is then used to carry out finite element simulations of micropillar compression of single crystals of two MAX phases, Ti₂AlC and Ti₃AlC₂. The finite element simulations not only quantitatively predict the stress – strain response of a wide range of crystallographic orientations of the micropillars but also rationalize the non-uniform deformation and the deformed shape of the micropillars observed in the experiments for the two materials. Parametric studies are also carried out to quantify the role of the non-Schmid effect and understand the effects of key experimental parameters on the stress – strain response of the micropillars of the two MAX phases.

1. Introduction

A family of ternary carbides and nitrides commonly referred to as MAX phases exhibit properties that combine some of the best attributes of both metals and ceramics (Barsoum, 2013; Barsoum and El-Raghy, 2001; Barsoum and Radovic, 2011; Radovic and Barsoum, 2013). Like ceramics these are lightweight, elastically stiff, thermodynamically stable and refractory, but also like metals these are damage tolerant, pseudo-ductile and machinable. The unique set of properties of MAX phases are in general associated with their atomically layered hexagonal crystal structure with a combination of strong intralayer and weak interlayer atomic bonds. Chemically, MAX phases are represented with by a general formula $M_{n+1}AX_n$, where 'M' is an early transition metal, 'A' mostly corresponds to elements from groups 13 to 16, 'X' is either carbon or nitrogen and 'n' varies from 1 to 3. In a $M_{n+1}AX_n$ crystal, 'M' elements are close-packed with 'X' atoms in the octahedral sites to form M_6X -octahedra in the $M_{n+1}X_n$ layers and these layers are separated by a single atomic layer of 'A' elements, while the value of 'n' in $M_{n+1}AX_n$ represents the stacking sequence i.e., when n=1, one $M_{n+1}X_n$ layer (or two M layers) are separated by the 'A' layers and so on. Also, these are one of the most diverse class of materials with already over 150 MAX phase compositions discovered and synthesized (Sokol et al., 2019).

The mechanical response of bulk polycrystalline MAX phases has been extensively characterized using conventional mechanical testing techniques which shows that MAX phases unlike their counterpart binary carbides and nitrides (MX), even at room temperature, undergo crystallographic slip on basal slip systems (Barsoum and El-Raghy, 1999; Barsoum et al., 1999a, 1999b; Farber, 1999;

E-mail address: ankit.sri@tamu.edu (A. Srivastava).

Editor: A.S. Khan

^{*} Corresponding author.

Farber et al., 1998). Several attempts have also been made to characterize the single-crystal level mechanical response of the MAX phases using grain-level nanoindentation tests (Barsoum et al., 2004; Griggs et al., 2017; Kooi et al., 2003; Molina-Aldareguia et al., 2003; Tromas et al., 2011) and uniaxial compression tests of micropillar specimens milled from individual grains (Brüsewitz et al., 2013; Higashi et al., 2018; Zhan et al., 2020; Zhan et al., 2021). The micropillar compression tests are particularly significant as they directly provide the crystallographic orientation dependent uniaxial stress-strain response of free-standing single crystals.

The results of the recent micropillar compression tests of $Ti_{n+1}AlC_n$ MAX phases by Zhan et al. (2020, 2021) have shown that the values of the resolved shear stress, τ_{RSS} , at the onset of crystallographic slip on basal slip systems (i.e., 'apparent' critical resolved shear stress, τ_{CRSS}) in MAX phases is highly orientation dependent. This is contrary to the classical Schmid law that predicts that the values of τ_{RSS} at the onset of crystallographic slip is independent of the crystallographic orientation. The non-Schmid orientation dependence of 'apparent' τ_{CRSS} for the MAX phase micropillars under compression in Zhan et al. (2020, 2021) was found to vary linearly with the compressive stress normal to the basal plane, σ_N . This relation can be written as, $\tau_{CRSS} = -\frac{k}{2}\sigma_N|\sin(\sigma_N) - 1| + \tau_0$, where k is the frictional resistance and τ_0 is the 'intrinsic' critical resolved shear stress for the onset of basal slip. Although, the crystallographic slip in the MAX phases is postulated to predominantly occur between the weakly bonded M-A layers (Gouriet et al., 2015) i.e., Ti-Al layers in $Ti_{n+1}AlC_n$ MAX phases, the difference in the stacking sequence, even between two $Ti_{n+1}AlC_n$ MAX phases i.e., Ti_3AlC_2 and Ti_2AlC , affects the Ti-Al bonds (Lane et al., 2013; Tan et al., 2014; Xiao et al., 2015). In line with this, a comparison of the non-Schmid crystallographic slip in Ti_3AlC_2 and Ti_2AlC micropillars by Zhan et al. (2021) also showed that the experimentally obtained values of τ_0 and k for the two MAX phases differ significantly.

The non-Schmid crystallographic slip is not unique to MAX phases and has also been reported and modelled for a host of other materials. For instance, non-Schmid crystal plasticity constitutive relations have been developed to describe anomalous crystallographic slip observed in several intermetallics (Ghorbanpour et al., 2020; Ghorbanpour et al., 2017; Gröger, 2021; Qin and Bassani, 1992), such as Ni₃Al, Ni₂Ga and Co₃Ti, and metallic materials, such as α-iron (Chen et al., 2014; Koester et al., 2012; Lim et al., 2015; Mapar et al., 2017; Patra et al., 2014; Srivastava et al., 2015), molybdenum and tungsten (Cereceda et al., 2016; Gröger et al., 2008a; Gröger et al., 2008b), chromium (Gröger and Vitek, 2020) and other body centered cubic (BCC) metallic materials (Knezevic et al., 2014; Weinberger et al., 2012). Borrowing concepts from these earlier works on intermetallics and BCC metallic materials, in this work, we present a non-Schmid crystal plasticity constitutive relation to model the crystallographic slip behavior observed in the two MAX phases, Ti₂AlC and Ti₃AlC₂ (Zhan et al., 2020; Zhan et al., 2021). We assume that the evolution of slip system resistance or strength in MAX phases has two components – a classical component that depends on the Taylor cumulative shear strain and a non-Schmid component that depends on the stress normal to the slip plane. However, it is observed that in order to quantitatively predict the experimentally obtained stress-strain response of the MAX phases, the non-Schmid slip system resistance in MAX phases must saturate once the stress normal to the slip systems reaches a critical value.

The values of the constitutive (material) parameters for the non-Schmid crystal plasticity constitutive relation formulated herein are either taken from the literature or are inferred from the results of the micropillar compression experiments of Zhan et al. (2020, 2021). The fully calibrated constitutive relation is then used to carry out finite element simulations of micropillar compression of both the MAX phases. The finite element simulations not only quantitatively predict the stress – strain response of a wide range of crystallographic orientations of the micropillars but also rationalize the non-uniform deformation and the deformed shape of the micropillars observed in the experiments for the two materials. Parametric studies are also carried out to quantify the role of the non-Schmid effect and understand the effects of two key experimental parameters – friction between the rigid punch and top surface of the micropillar, and the vertical taper of the micropillars – on the mechanical response of the micropillars of the two materials.

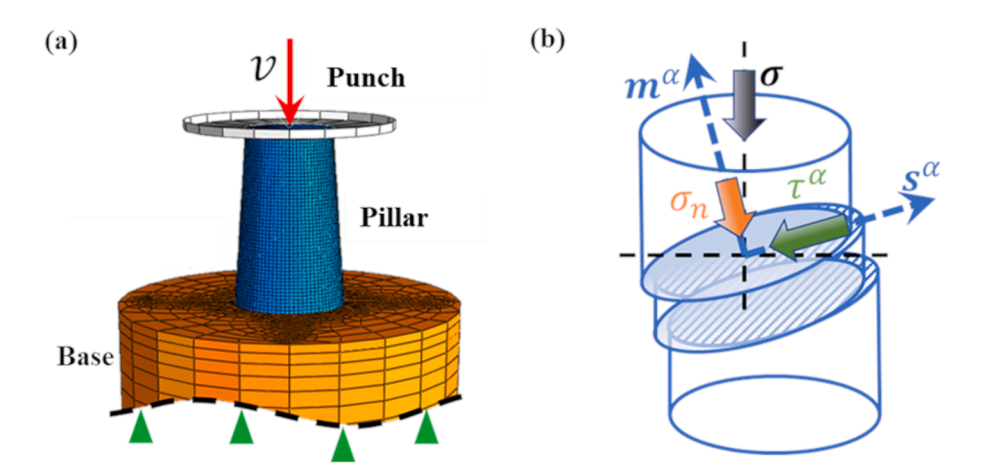


Fig. 1. (a) A schematic showing a typical finite element model of the micropillar specimen attached to a base and being compressed along the axis using a punch. (b) A schematic showing applied stress, σ , on a cylindrical specimen, resultant normal stress, σ_n , acting on the slip plane with plane normal, m^{α} , and the resolved shear stress, τ^{α} , acting on the same slip plane in the slip direction, s^{α} .

2. Crystal plasticity finite element modeling

2.1. Finite element model

The finite element model considered here mimics the micropillar compression experiments of Zhan et al. (2020, 2021). A typical finite element model is shown in Fig. 1(a) that contains a micropillar attached to the base material and is compressed along the axis using a punch. As in the experiments, the diameter of the micropillar is taken to be $10 \mu m$ and the height to (top) diameter ratio of the micropillar is taken to be 2 with a vertical taper of 5° (unless stated otherwise). The diameter of the base is taken to be 4 times and the height of the base is taken to be 3 times that of the micropillar. This is in line with the experiments where the micropillar specimens milled from a large grain is still attached to the base material during the compression tests. The micropillar and base are discretized using C3D8 elements with reduced integration of the ABAQUS/Standard, 2020 element library while the punch is modeled as a discrete rigid body. A surface-surface contact with a coefficient of friction 0.1 (unless stated otherwise) is invoked between the rigid punch and top surface of the micropillar. The punch is constrained in the in-plane directions and is subjected to a uniaxial velocity along the axis of the micropillar while the bottom of the base is constrained in both in-plane and out-of-plane directions.

2.2. Field equations

We describe the deformation in the usual way i.e., a point originally located at X moves to a new position x = X + u(X) in the deformed configuration and the local deformation of an infinitesimal volume element at a position X in the undeformed configuration is characterized by the deformation gradient, $F = \partial x/\partial X$. The total deformation gradient is then multiplicatively decomposed into its elastic part, F^e , arising from the reversible deformation of the lattice, and the plastic part, F^p , which accounts for crystallographic slip in the crystal as, $F = F^e F^p$. Following this, the strain rate, $\dot{\varepsilon} = \text{sym}(\partial \dot{x}/\partial X)$, is decomposed into its elastic and plastic parts as

$$\dot{\boldsymbol{\varepsilon}} = \dot{\boldsymbol{\varepsilon}}^e + \dot{\boldsymbol{\varepsilon}}^p; \ \dot{\boldsymbol{\varepsilon}}^e = \operatorname{sym}(\dot{\boldsymbol{F}}^e \boldsymbol{F}^{-1}); \ \dot{\boldsymbol{\varepsilon}}^p = \operatorname{sym}(\boldsymbol{F}^e \dot{\boldsymbol{F}}^p \boldsymbol{F}^{p-1} \boldsymbol{F}^{e-1})$$
(1)

We also introduce the elastic Lagrange strain tensor, $E^e = 1/2$ ($F^{eT}F^e - I$) to define the reversible deformation of the crystal lattice. Next, the Cauchy (true) stress tensor, σ_{\bullet} that satisfies the equilibrium condition, $\partial \sigma / \partial x = 0$, is related to the elastic strain as

$$\sigma = \frac{1}{I} F^{e} [\mathbb{C} : E^{e}] F^{eT}$$
 (2)

where, $J = \det(F)$, and \mathbb{C} is the fourth-order anisotropic elastic moduli tensor of the material in the undeformed configuration. In order to complete the governing equations, a constitutive equation is required which relates the plastic strain rate, $\dot{\varepsilon}^p$, to the stress, σ , and is described in the following section.

2.3. Crystal plasticity constitutive relation

The room temperature crystallographic slip activity in the MAX phases is limited to the basal, $\{0001\}\langle11\overline{2}0\rangle$, slip systems (Barsoum et al., 1999a; Gouriet et al., 2015; Guitton et al., 2012); and as shown schematically in Fig. 1(b), we define the slip direction and slip plane normal for a basal slip system, α , in the undeformed configuration using unit vectors s^{α} and m^{α} , respectively. These can be transformed to the current deformed configuration using $s^{*\alpha} = F^e s^{\alpha}$ and $m^{*\alpha} = m^{\alpha} F^{e-1}$. The plastic strain rate in Eq. (1) is then defined in terms of the shear strain rate on the α^{th} slip system i.e., $\dot{\gamma}^{\alpha}$ as

$$\dot{\boldsymbol{\varepsilon}}^p = \sum_{\alpha} \dot{\boldsymbol{\gamma}}^\alpha \operatorname{sym}(s^{*\alpha} \otimes \boldsymbol{m}^{*\alpha}) \tag{3}$$

where, the shear strain-rate, $\dot{\gamma}^{\alpha}$, is given by

$$\dot{\gamma}^{\alpha} = \dot{\gamma}_0 \left(\frac{|\tau^{\alpha}|}{g^{\alpha}} \right)^{\frac{1}{m}} \operatorname{sign}(\tau^{\alpha}) \tag{4}$$

with $\dot{\gamma}_0$ and m being the reference shear strain-rate and strain-rate sensitivity, respectively, $\tau^a = \sigma : (s^{*a} \otimes m^{*a})$ being the resolved shear stress which is the driving force for slip and g^a is the current slip system strength or simply the resistance to slip. Recall that the experimental results show that the values of the resolved shear stress at the onset of crystallographic slip i.e., the 'apparent' critical resolved shear stress, τ_{CRSS} , which is basically the slip system strength, g^a , at the onset of crystallographic slip for MAX phases follows, $\tau_{CRSS} = -\frac{k}{2}\sigma_N |\sin(\sigma_N) - 1| + \tau_0$ (Zhan et al., 2020, 2021). In this relation, τ_0 is the 'intrinsic' critical resolved shear stress of the material and can be assumed to evolve with the cumulative shear strain as in classical strain-hardening of crystals, while the first term, $-\frac{k}{2}\sigma_N |\sin(\sigma_N) - 1|$, represents the current non-Schmid slip system resistance.

Following this, we assume that the slip system resistance, g^{α} , in Eq. (4) is a sum of the classical, g^{α}_{γ} , and non-Schmid, g^{α}_{N} , slip system strength/resistance i.e., $g^{\alpha} = g^{\alpha}_{\gamma} + g^{\alpha}_{n}$. The classical slip system strength is assumed to evolve according to (Peirce et al., 1982)

$$g_{\gamma}^{\alpha} = \sum_{\beta} h_{\alpha\beta} |\dot{\gamma}^{\beta}| \tag{5}$$

and the hardening moduli follows

$$h_{\alpha\beta} = qh_{\alpha\alpha}, \ h_{\alpha\alpha} = h_0 \operatorname{sech}^2\left(\frac{h_0\overline{\gamma}}{\tau_s - \tau_0}\right), \ \overline{\gamma} = \sum_{\alpha} \int_0^t |\dot{\gamma}^{\alpha}| dt$$
 (6)

with q, h_0 and τ_s being the constitutive parameters. The value of $g_{\gamma}^a = \tau_0$ at time, t = 0, where τ_0 is the 'intrinsic' critical resolved shear stress for the basal slip as identified from the micropillar compression experiments (Zhan et al., 2020, 2021).

Next, the evolution of the non-Schmid slip system resistance, g_N^{α} , that depends on the component of the stress normal to the basal plane, σ_N , as schematically shown in Fig. 1(b), follows from the experimental observations, however, with a slight modification as

$$\dot{g}_N^a = -\left(\frac{k}{2}\right) \dot{\sigma}_N |\operatorname{sign}(\sigma_N) - 1| \mathbf{H}(\sigma_N^c - |\sigma_N|) \tag{7}$$

where, $\sigma_N = \sigma : (m^{*1} \otimes m^{*1})$ and k is the frictional resistance for the basal slip as identified from the micropillar compression experiments (Zhan et al., 2020, 2021). The function $H(\blacksquare)$ in Eq. (7) is the Heaviside step function

$$H(x) = \begin{cases} 0, & x < 0 \\ 1, & x > 0 \end{cases}$$
 (8)

The use of the Heaviside step function ensures that the non-Schmid slip resistance, g_N^α , only evolves when the magnitude of the stress normal to the slip system, $|\sigma_N|$, is less than a critical value, σ_N^c . Also, the value of $g_N^\alpha = 0$ at time, t = 0, since initially the micropillars are stress free. The Heaviside function in Eq. (7) was needed to reproduce the experimentally obtained stress-strain response of the MAX phases. Note that in Zhan et al. (2020, 2021) the dependence of τ_{CRSS} on σ_N was only analyzed at the onset of plastic deformation and the influence of the non-Schmid effect on the evolution of the stress-strain response of the micropillars was not considered. Nevertheless, we have also carried out parametric studies highlighting the role of σ_N^c in Section 3.2.

The crystal plasticity constitutive relation incorporating the non-Schmid effect on the crystallographic slip of MAX phases described above is implemented as user material subroutine (UMAT) in the ABAQUS/Standard, 2020. The UMAT is based on the work of Huang (1991) and follows the constitutive formulation detailed in Asaro and Needleman (1985).

3. Results

The non-Schmid crystal plasticity constitutive relation formulated in Section 2.3 has several constitutive (material) parameters that need to be determined. These include the elastic constants as well as the constitutive parameters in Eqs. (4), (6) and (7). The elastic constants for the Ti₂AlC and Ti₃AlC₂ MAX phases are taken from the work of Du et al. (2009) and Wang and Zhou (2004), respectively. For both the MAX phases, the value of $\dot{\gamma}_0$ is taken to be similar to the nominal strain rate imposed in the experiments (Zhan et al., 2020; Zhan et al., 2021), m is taken to be 50 to capture the slight rate-dependence in the mechanical response of these materials (Bhatta-charya et al., 2014), and the value of q is taken to be 1. Also, for both the MAX phases, the values of τ_0 and k are directly obtained from the micropillar compression experiments (Zhan et al., 2020, 2021).

Finally, the values of the remaining three parameters, h_0 , τ_s and σ_N^c are obtained using an iterative optimization process involving full three-dimensional finite element simulations of selected micropillar compression experiments for both the MAX phases. The iterative optimization process follows Nelder-Mead (Lagarias et al., 1998) algorithm that minimizes the mean squared error between the nominal compressive stress-plastic strain responses obtained from the micropillar compression experiments and the analogous finite element simulations. To this end, two crystallographic orientations are selected for each of the MAX phases. The calibrated values of all the constitutive parameters for both the MAX phases are given in Table 1.

3.1. Comparison with the micropillar experiments

The nominal compressive stress – plastic strain response of four single crystal micropillars of each of the MAX phase i.e., Ti₂AlC and Ti₃AlC₂, obtained using the proposed fully calibrated non-Schmid crystal plasticity constitutive relation is compared with the experimental results of Zhan et al. (2020, 2021) in Fig. 2. The cases shown in Fig. 2(a,b) were used for calibration of the constitutive

Table 1
The values of the constitutive parameters for Ti₂AlC and Ti₃AlC₂ MAX phases.

Elastic constar	nts:							
	C_{11} [GPa]	C_{12} [C	GPa]	C_{13} [GPa]	C_{33} [GPa]	C_{44} [C	GPa]	
Ti ₂ AlC	302	59		55	278	113		
Ti_3AlC_2	361	75		70	299	124		
Constitutive p	arameters in Eqs. (4),	(6) and (7):						
	$\dot{\gamma}_0~[\mathrm{s}^{-1}]$	m	q	h_0 [MPa]	$ au_0 \; [ext{MPa}]$	$ au_s$ [MPa]	k	$\sigma_N^c \; [ext{MPa}]$
Ti ₂ AlC	0.01	50	1	616	13.8	332	0.28	120.6
Ti_3AlC_2	0.01	50	1	1615	19.6	65	0.20	130.2

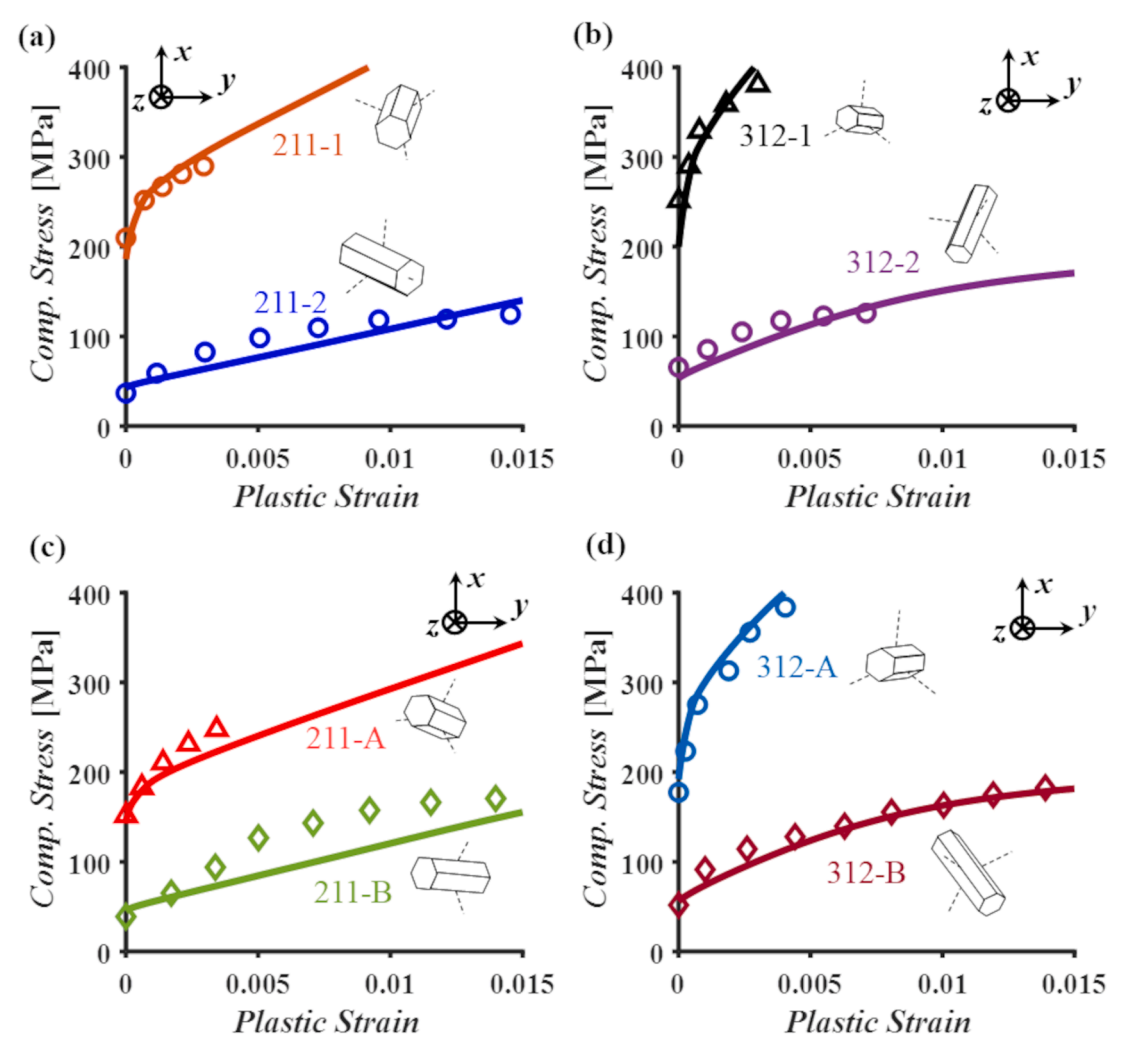


Fig. 2. A comparison of the experimental (Zhan et al., 2020, 2021) and predicted nominal compressive (Comp.) stress – plastic strain response of two micropillars of (a) Ti_2AlC and (b) Ti_3AlC_2 MAX phases used for calibrating the constitutive parameters, and that of the experimental (Zhan et al., 2020, 2021) and predicted nominal compressive (Comp.) stress – plastic strain response of two micropillars of (c) Ti_2AlC and (d) Ti_3AlC_2 MAX phases that were not used for calibration. The experimental data are shown using open symbols while the predicted curves are shown using solid lines. The crystallographic orientations of the micropillars in terms of Euler angles (in degrees using Bunge convention) are: (161, 159, 32), (65, 44, 56), (68, 155, 35) and (85, 139, 59) for 211-1, 211-2, 211-A and 211-B, respectively, and (84, 161, 30), (157, 129, 6), (97, 162, 43) and (37, 56, 11) for 312-1, 312-2, 312-A and 312-B, respectively.

parameters while those shown in Fig. 2(c,d) are predictions. As can be seen in the figure, the predicted nominal compressive stress – plastic strain response is in very good agreement with the experimental results. Note that the micropillars in Fig. 2 cover a wide range of crystallographic orientations as shown schematically using the unit cell representations of the crystallographic orientations of the hexagonal single crystals in the figure.

Fig. 3 compares the predicted and experimentally obtained (Zhan et al., 2020, 2021) variation of the 'apparent' critical resolved shear stress, τ_{CRSS} , with the component of the stress normal to the basal plane, σ_N , for a wide range of crystallographic orientations of the single crystal micropillars of both Ti₂AlC and Ti₃AlC₂ MAX phases. Here, $\tau_{CRSS} = \sigma_y \cos\phi\cos\lambda$ and $\sigma_N = \sigma_y \cos^2\phi$, with σ_y being the 0.015% offset yield strength (Zhan et al., 2020, 2021), ϕ being the angle between the loading direction and the basal plane normal, and λ being the angle between the loading direction and the active slip direction. The crystallographic orientations of all the micropillars considered in Fig. 3 are given in Table 2. Recall, that Zhan et al. (2020, 2021) found that for the MAX phases, 'apparent' τ_{CRSS} varies linearly with σ_N (at least for $\sigma_N < 0$). As can be seen in Fig. 3, consistent with the experimental observations the predicted variation of τ_{CRSS} with $|\sigma_N|$ for both the MAX phases also follow the same linear dependence.

We also plot the variation of the macroscopic yield strength, σ_y , of single crystal micropillars of both Ti₂AlC and Ti₃AlC₂ MAX phases predicted using the proposed non-Schmid crystal plasticity constitutive relation, σ_y^{CPFE} , with the values obtained from the micropillar compression experiments (Zhan et al., 2020, 2021), σ_y^{Exp} , in Fig. 4. The crystallographic orientations of all the micropillars

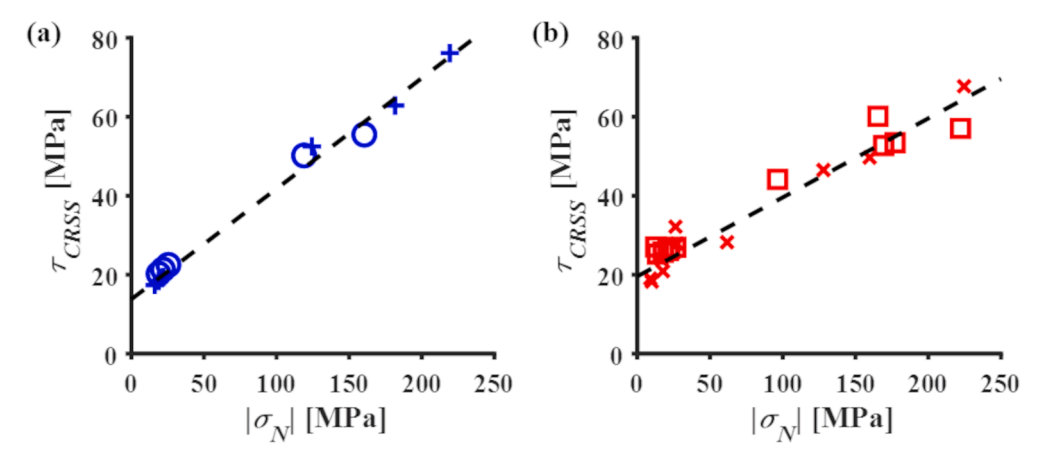


Fig. 3. A comparison of the experimental (+/x symbols) and predicted (open circles and squares) variation of the 'apparent' critical resolved shear stress, τ_{CRSS} , with the component of stress normal to the basal plane, σ_N , for the micropillars of (a) Ti₂AlC and (b) Ti₃AlC₂ MAX phases. The experimental data is taken from the work of Zhan et al. (2020, 2021).

Table 2
The crystallographic orientations (in terms of Euler angles in degrees using Bunge convention) of all the single crystal micropillars of Ti_2AlC and Ti_3AlC_2 MAX phases used in the experimental study of Zhan et al. (2020, 2021).

Ti ₂ AlC			Ti_3AlC_2		_
φ_1	ϕ	$arphi_2$	$arphi_1$	ϕ	$arphi_2$
75	86	7	119	67	20
168	80	37	49	119	1
163	47	60	37	56	11
65	44	56	116	52	22
85	139	59	157	129	6
68	155	35	86	134	3
161	159	32	96	25	51
137	161	1	177	160	1
			84	161	30
			97	162	43
			52	166	59

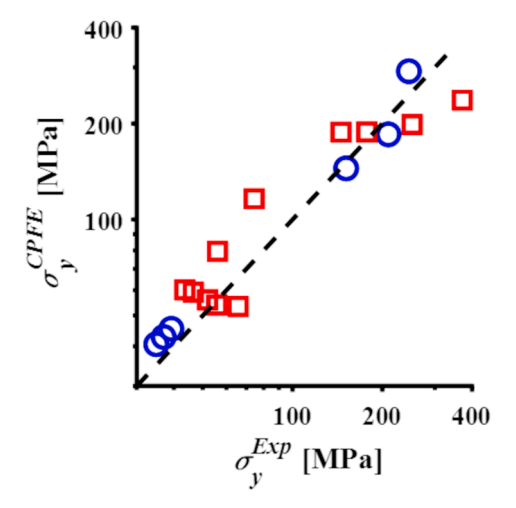


Fig. 4. A comparison of the experimental (Exp) and predicted (CPFE) yield strength, σ_y , of the Ti₂AlC (open circles) and Ti₃AlC₂ (open squares) MAX phase micropillars with a wide range of crystallographic orientations. The results are shown on a log-log plot. The experimental data is taken from the work of Zhan et al. (2020, 2021).

considered in Fig. 4 are given in Table 2. As can be seen in Fig. 4, all the values lie along a straight line with a slope of 45°, demonstrating the good agreement between the predicted and experimentally obtained values of the macroscopic yield strength of single crystal micropillars with a wide range of crystallographic orientations.

Next, in Figs. 5 and 6 we compare the deformed shapes of a few micropillars of Ti₂AlC and Ti₃AlC₂ MAX phases, respectively, from the experimental work of Zhan et al. (2020, 2021) with the predicted distribution of Taylor cumulative shear strain, $\bar{\gamma} = \sum \int_0^t |\dot{\gamma}^a| dt$, in

the micropillars. Note that the post-deformation observation of the micropillars in Zhan et al. (2020, 2021) was made after a large amount of imposed compressive deformation while the contour plots of $\bar{\gamma}$ from the crystal plasticity finite element simulations are plotted at an imposed nominal compressive strain of 0.02. Also, in Figs. 5 and 6, for the finite element results, the base material and the rigid punch are purposefully hidden to highlight the predicted deformation pattern in the micropillars.

As can be seen in Fig. 5, the two micropillars of Ti₂AlC MAX phase in the experiments, Fig. 5(a,c), underwent non-uniform deformation on multiple parallel slip planes as evident from the remnant slip markings on the deformed micropillars. Also, since the crystallographic orientation of the two micropillars are different (a schematic representation of the crystallographic orientation of the hexagonal unit cell are also shown in the figure), the orientation of the remnant slip markings with respect to the loading axis in these two micropillars are also different. Similar observations can be made for the two experimentally deformed micropillars of Ti_3AlC_2 MAX phase shown in Fig. 6(a,c). The contour plots of $\overline{\gamma}$ obtained from the finite element simulations using the proposed non-Schmid crystal plasticity constitutive relation in the two Ti₂AlC MAX phase micropillars are shown in Fig. 5(b,d) while the same in the two Ti₃AlC₂ MAX phase are shown in Fig. 6(b,d). Although the contour plots in Figs. 5 and 6 show the distribution of $\overline{\gamma}$, we note that for these micropillars, crystallographic slip predominantly occurs on a single slip system in most of the micropillars except for the case shown in Fig. 5(a) where two slip systems are simultaneously active throughout the deformation process. Nevertheless, the distribution of $\bar{\gamma}$ is expected to represent the overall deformation in the micropillars. In line with this, a visual comparison of the shapes of the experimentally deformed micropillars with the predicted contour plots of $\bar{\gamma}$ in the same micropillars clearly shows that the predicted distribution of $\bar{\gamma}$ very well captures the non-uniform deformation of the micropillars. The visual comparison also reveals that the inclinations of the predicted isocontours of $\overline{\gamma}$ are in line with the inclinations of the remnant slip markings seen in the experimentally deformed micropillars. More importantly, the predicted deformed shapes in Figs. 5(b) and 6(b) clearly show the propensity to bend for these micropillars in line with the bending of the micropillars observed in the experiments, see Figs. 5(a) and 6(a).

3.2. Role of the non-Schmid effect

It is instructive to analyze the impact of the non-Schmid effect on the stress-strain response of both the MAX phases, Ti₂AlC and Ti₃AlC₂. To this end, we focus on three single crystal micropillars with basal plane (0001) normal inclined at 80°, 30° and 45° with respect to the loading axis or simply the axis of the micropillars. A schematic representation of the crystallographic orientation of the three hexagonal unit cells (labeled A, B and C for Ti₂AlC, and I, II and III for Ti₃AlC₂, respectively) are shown in the Figs. 7 and 8 as insets. The maximum Schmid factor, $\max(s^{*\alpha} \otimes m^{*\alpha})$, that dictates the resolved shear stress on the active slip system in these three micropillars (labeled A, B and C or I, II and III) are 0.17, 0.43 and 0.5, respectively, while the maximum normal factor, $\max(m^{*\alpha} \otimes m^{*\alpha})$, that dictates the non-Schmid effect in the three micropillars are 0.03, 0.75 and 0.5, respectively.

We now compare the stress-strain response of the three micropillars of both the MAX phases, with and without non-Schmid effect, in Fig. 7. As can be seen in the figure, the difference between the stress-strain response of the micropillars with and without non-Schmid effect strongly depends on the crystallographic orientation of the micropillars, for both the MAX phases. The micropillars with low values of the maximum Schmid factor i.e., A and I, in Fig. 7(a,b), have relatively high compressive yield strength and post-yielding these undergo limited plastic deformation. More importantly, since the values of the normal factor for these micropillars are also low, the impact of the non-Schmid effect on the stress-strain response of these micropillars is almost negligible. However, for crystallographic orientations with sufficiently greater values of the Schmid and normal factors, the non-Schmid effect significantly affects the stress-strain response of the micropillars as can be seen for micropillars B, C, II and III. Such that, neglecting non-Schmid effect for

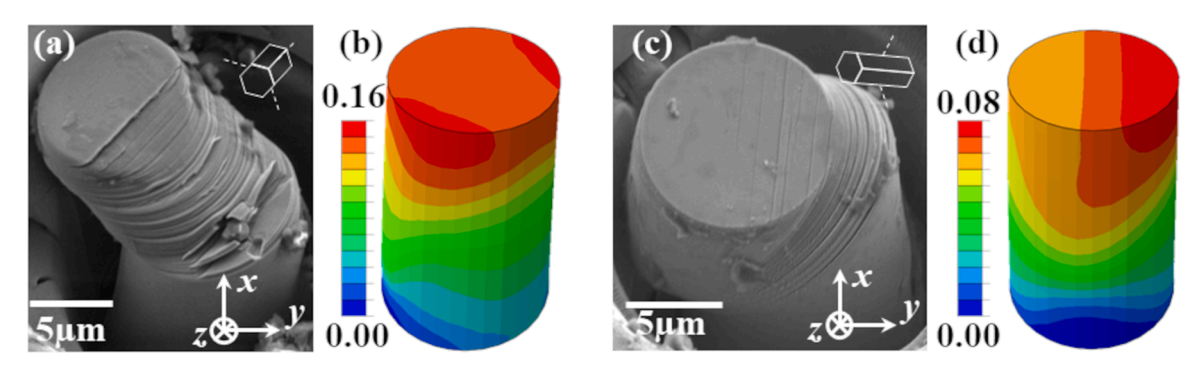


Fig. 5. SE-SEM images of deformed micropillars and corresponding predicted variation of the Taylor cumulative shear strain for Ti_2AlC micropillars with crystallographic orientations in terms of Euler angles (in degrees using Bunge convention): (a,b) (137, 161, 1) and (c,d) (85, 139, 59). The SE-SEM images of the deformed micropillars are taken from the work of Zhan et al. (2020).

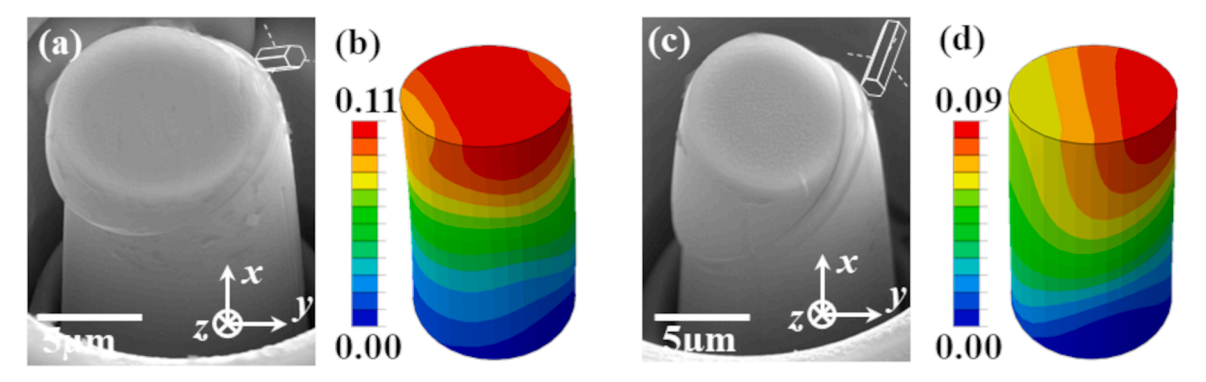


Fig. 6. SE-SEM images of deformed micropillars and corresponding predicted variation of the Taylor cumulative shear strain for Ti_3AlC_2 micropillars with crystallographic orientations in terms of Euler angles (in degrees using Bunge convention): (a,b) (96, 25, 51) and (c,d) (157, 129, 6). The SE-SEM images of the deformed micropillars are taken from the work of Zhan et al. (2021).

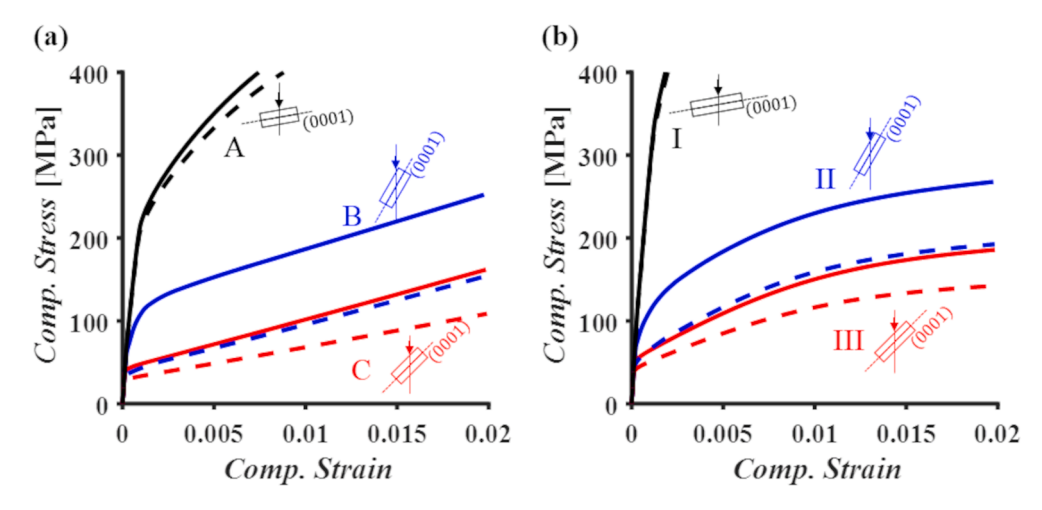


Fig. 7. A comparison of the predicted nominal compressive (Comp.) stress – strain response of three micropillars of (a) Ti₂AlC and (b) Ti₃AlC₂ MAX phases with (solid lines) and without (dashed lines) non-Schmid effect. The crystallographic orientations of the micropillars in terms of Euler angles (in degrees using Bunge convention) are: (90, 80, 300), (90, 30, 300) and (90, 45, 300) for micropillars A, B and C (or I, II and III), respectively.

these micropillars results in relatively lower values of the initial yield stress as well as lower values of the flow stress throughout the deformation. The impact of the non-Schmid effect on the stress-strain response of the micropillars with sufficiently greater values of the Schmid and normal factors, depends on the value of the normal factor. For example, the impact of the non-Schmid effect is greater on the micropillars with the value of the normal factor being 0.75 (i.e., B and II) compared to the micropillars with the value of the normal factor being 0. 5 (i.e., C and III). Furthermore, the impact of the non-Schmid effect on the stress-strain response of the micropillars is greater for the Ti₂AlC MAX phase compared to the Ti₃AlC₂ MAX phase.

Recall that in Eq. (7) it is assumed that the current non-Schmid slip system resistance, g_N^α , only evolves while the stress normal to the slip systems is less than a critical value, σ_N^c . This was needed to reproduce the experimentally obtained stress-strain response of the MAX phases. Nevertheless, we now analyze the effect of the finite value of σ_N^c on the stress-strain response of both the MAX phases. To this end, we consider the same three single crystal micropillars with basal plane (0001) normal inclined at 80°, 30° and 45° with respect to the loading axis as in Fig. 7. The stress-strain response of these three micropillars of both the MAX phases, with a finite value of σ_N^c (given in Table 1) and with $\sigma_N^c \to \infty$ are compared in Fig. 8. A very large value of σ_N^c guarantees that the value of the Heaviside step function in Eq. (7) is one throughout the deformation for all the micropillars. As can be seen in Fig. 8, the impact of limiting the extent of non-Schmid effect by introducing a finite value of σ_N^c on the stress-strain response of the micropillars strongly depends on the crystallographic orientation of the micropillars for both the MAX phases. For crystallographic orientations with low values of the normal factor or very high values of the Schmid factor, such as micropillars A and C, and I and III in Fig. 8(a) and (b), respectively, the impact of limiting the extent of non-Schmid effect on the stress-strain response is rather negligible. However, for micropillars B and II, for which the value of the normal factor is rather high, not limiting the extent of the non-Schmid effect significantly overestimates their flow stress.

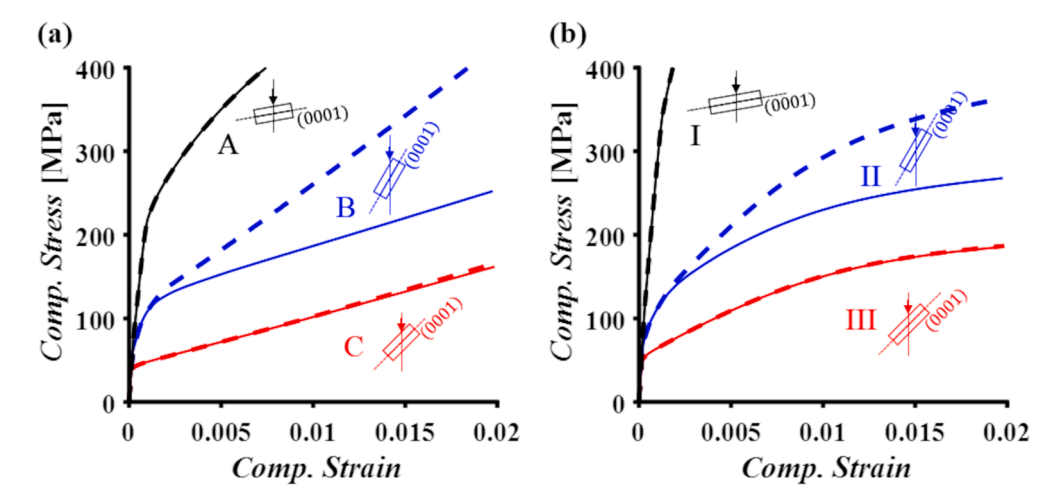


Fig. 8. A comparison of the predicted nominal compressive (Comp.) stress – strain response of three micropillars of (a) Ti₂AlC and (b) Ti₃AlC₂ MAX phases with the values of σ_N^c given in Table 1 (solid lines) and assuming $\sigma_N^c \to \infty$ (dashed lines). The crystallographic orientations of the micropillars in terms of Euler angles (in degrees using Bunge convention) are: (90, 80, 300), (90, 30, 300) and (90, 45, 300) for micropillars A, B and C (or I, II and III), respectively.

3.3. Influence of key experimental parameters

In this section, we analyze the effects of two key experimental parameters – friction between the rigid punch and top surface of the micropillar, and the vertical taper of the micropillars. The coefficient of friction between the rigid punch and top surface of the micropillar is not directly known from the experiments of Zhan et al. (2020, 2021) and thus far in all our simulations the value of the coefficient of friction is taken to be 0.1. This small value of 0.1 is assumed based on the considerable sliding between the micropillar and punch in the experiments as evident from the deformed shapes of the micropillars in Figs. 5 and 6. Also, the coefficient of friction between a rigid probe and MAX phases is found be as low as \sim 0.1 at room temperature (Smith et al., 2013). Nevertheless, it is warranted to analyze the effect of friction between the rigid punch and top surface of the micropillars on their predicted stress-strain response. To this end, we consider the same three single crystal micropillars with basal plane (0001) normal inclined at 80°, 30° and 45° with respect to the loading axis as in Section 3.2.

The stress-strain response of these three micropillars of both the MAX phases, with coefficient of friction between the punch and the micropillars being 0.1 and 0.3 are compared in Fig. 9. As can be seen in the figure, the effect of friction between the punch and the micropillars on their stress-strain response strongly depends on their crystallographic orientation for both the MAX phases. For micropillars A and B, and I and II in Fig. 9(a) and (b), respectively, an increase in the friction overestimates their flow stress, while for

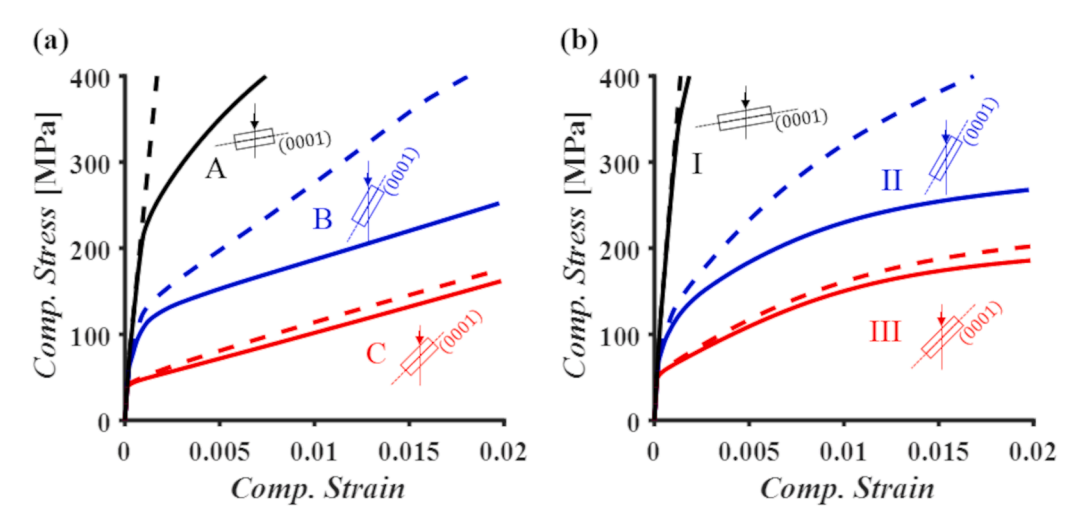


Fig. 9. A comparison of the predicted nominal compressive (Comp.) stress – strain response of three micropillars of (a) Ti₂AlC and (b) Ti₃AlC₂ MAX phases with coefficient of friction between the punch and the micropillars being 0.1 (solid lines) and 0.3 (dashed lines). The crystallographic orientations of the micropillars in terms of Euler angles (in degrees using Bunge convention) are: (90, 80, 300), (90, 30, 300) and (90, 45, 300) for micropillars A, B and C (or I, II and III), respectively.

micropillars C and III, friction has a rather negligible effect on their stress-strain response. The significant effect of friction on the stress-strain response of the micropillars A and I is due to the fact that in these micropillars the basal planes are roughly parallel to the loading axis, so that, a greater friction between the punch and the micropillar introduces a constraint normal to the basal plane which in turn increases the value of σ_N , even though the value of the normal factor is only 0.03 for these micropillars. On the contrary, the significant effect of friction on the stress-strain response of the micropillars B and II (for which the value of the Schmid factor is 0.43 and that of the normal factor is 0.75) is because these micropillars tend to bend during compression (see Figs. 5(a) and 6(a) which show the deformed shape of the micropillars with similar orientation of the basal planes as in B and II) but a greater friction restricts the sliding between the punch and the micropillar which in turn restricts the overall bending of the micropillars.

Next, we analyze the effect of the vertical taper of the micropillars on their stress-strain response. Here as well, we consider the same three single crystal micropillars with basal plane (0001) normal inclined at 80° , 30° and 45° with respect to the loading axis as in Fig. 9. The stress-strain response of these three micropillars of both the MAX phases, with a vertical taper of 0° and 5° are compared in Fig. 10. As can be seen in the figure, for the dimensions of the micropillars considered in this work, there is only a small effect of the vertical taper on the initial yield strength. However, the presence of a small taper in the micropillars slightly increases the flow stress.

4. Discussion

We have formulated a non-Schmid crystal plasticity constitutive relation to model crystallographic slip in MAX phases. This was motivated by the experimental observations that unlike the materials that follow the classical Schmid law, the values of the resolved shear stress at the onset of crystallographic slip on basal slip systems in MAX phases is highly orientation dependent (Zhan et al., 2020, 2021). Next, we carried out finite element simulations of micropillar compression of Ti₂AlC and Ti₃AlC₂ MAX phases using the proposed constitutive relation and compared the predictions with the experimental results. Our results show that the predicted stress – strain response of a wide range of crystallographic orientations of the micropillars for both the MAX phases are in very good quantitative agreement with the experimental results. Furthermore, the predicted distribution of Taylor cumulative shear strain in the micropillars are found to not only capture the onset of non-uniform deformation but also to an extent rationalize the deformed shapes of the micropillars observed in the experiments for both the MAX phases.

The non-Schmid effects on the crystallographic slip has been previously incorporated within classical crystal plasticity constitutive relations for intermetallics (Ghorbanpour et al., 2020; Ghorbanpour et al., 2017; Gröger, 2021; Qin and Bassani, 1992) and BCC metallic material (Cereceda et al., 2016; Chen et al., 2014; Gröger et al., 2008a; Gröger et al., 2008b; Gröger and Vitek, 2020; Knezevic et al., 2014; Koester et al., 2012; Lim et al., 2015; Mapar et al., 2017; Patra et al., 2014; Srivastava et al., 2015; Weinberger et al., 2012) by accounting for the effects of stresses other than the resolved shear stresses on the slip systems. For example, for intermetallics with L12 crystal structure, Qin and Bassani (1992) added the contribution of shear stresses on $\{100\}$ cross-slip planes in the $\langle 0\overline{1}1\rangle$ directions to the resolved shear stresses on the $\{111\}\langle 0\overline{1}1\rangle$ slip systems. Similarly, in BCC metals where it is widely accepted that the non-planar spreading of the screw dislocation core in the presence of stresses other than the resolved shear stress leads to non-Schmid effect (Duesbery and Vitek, 1998), the effective resolved shear stress on a slip system is taken as a linear combination of various components of the stresses with coefficients representing the relative effect of each component (Gröger, 2021; Gröger et al., 2008b; Knezevic et al., 2014; Koester et al., 2012; Lim et al., 2015). Alternatively, instead of modifying the resolved shear stress (i.e., the driving force for slip), Chen et al. (2014), within a fully rate-dependent crystal plasticity formulation simply modified the evolution of the slip system strength

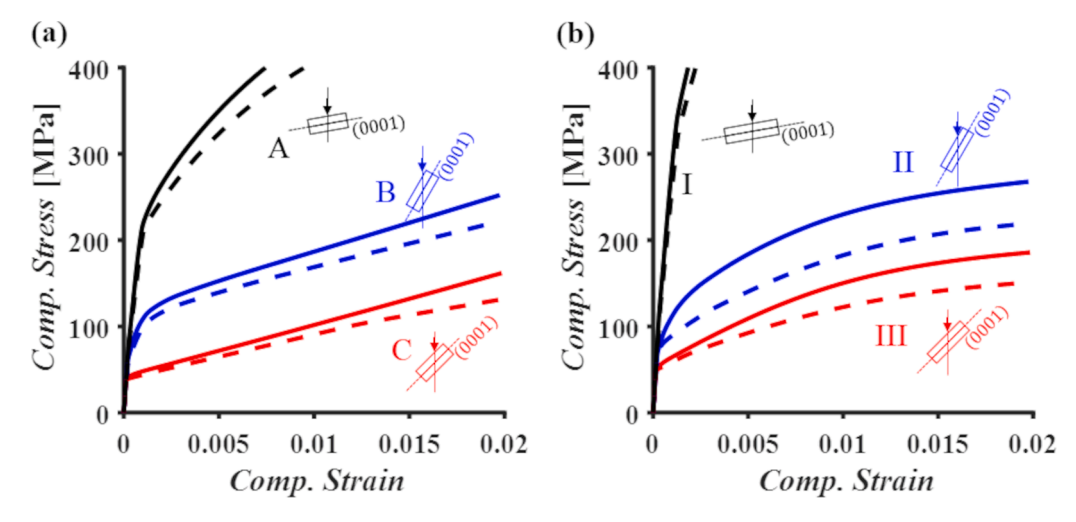


Fig. 10. A comparison of the predicted nominal compressive (Comp.) stress – strain response of three micropillars of (a) Ti_2AlC and (b) Ti_3AlC_2 MAX phases with a vertical taper of 5° (solid lines) and 0° (dashed lines). The crystallographic orientations of the micropillars in terms of Euler angles (in degrees using Bunge convention) are: (90, 80, 300), (90, 30, 300) and (90, 45, 300) for micropillars A, B and C (or I, II and III), respectively.

(i.e., the resistance to slip) to account for the non-Schmid effects. The non-Schmid effects incorporated in Chen et al. (2014) followed from the prior works on non-Schmid crystal plasticity yield criteria and flow rules (Gröger et al., 2008b; Koester et al., 2012).

Here we assumed that the evolution of the resistance to slip or simply the slip system strength, g^{α} , in MAX phases is the sum of a classical component, g^{α}_{γ} , that depends on the Taylor cumulative shear strain and a non-Schmid component, g^{α}_{γ} , that depends on the stress normal to the slip plane, σ_N . So that the non-Schmid effect in our formulation enters in the denominator of Eq. (4) as in Chen et al. (2014) and not in the numerator as in Knezevic et al. (2014). Where to introduce the non-Schmid effect in Eq. (4) is a constitutive choice, however, in the rate-independent limit i.e., $m \to 0$, both our choice and that of Knezevic et al. (2014) will reduce to that of Qin and Bassani (1992), and others. Also, when $\dot{\gamma}^{\alpha} \to \dot{\gamma}_0$ (i.e., the material rate of shear approaches the reference rate), both our choice and that of Knezevic et al. (2014) are mathematically the same. Nevertheless, note that incorporating the non-Schmid effect in the numerator affects the driving force for slip while incorporating it in the denominator affects the resistance to slip. So that if the non-Schmid effect is incorporated in the numerator it can give rise to erroneous slip when the non-Schmid component is much greater than the resolved shear stress and their difference exceeds the current value of g^{α}_{γ} , for instance, in the presence of excess compressive hydrostatic pressure on the specimen. More importantly, both the stress components, τ^{α} and σ_N , involved in describing the shear strain rate in Eq. (4) obey the inversion symmetry in line with the discussion in Gröger (2021).

Although the atomic origin of non-Schmid effect in MAX phases is not yet known it is safe to say that they differ from the BCC metals. Recent atomistic simulation results have indeed shown that in MAX phases where crystallographic slip occurs due to basal dislocations, the core structure of these dislocations is not affected by the normal stresses (Plummer et al., 2022). Nevertheless, since the dislocation activities are confined to basal planes in MAX phases, it can lead to strong dislocation interactions and alignments along specific orientation thus resulting in increased lattice friction (Guitton et al., 2012), which can give rise to non-Schmid effects in line with the description of slip system resistance assumed in this work.

Furthermore, unlike the prior works on non-Schmid crystallographic slip, here we found that in order to quantitatively predict the experimentally obtained stress-strain response of the MAX phases, the non-Schmid slip system resistance must saturate once the stress normal to the slip planes reaches a critical value. It is also worth noting that as per Eq. (7), the value of g_N^a is only positive when both σ_N and $\dot{\sigma}_N$ are negative, and the non-Schmid resistance to slip, g_N^a , continues to increase (until $|\sigma_N| < \sigma_N^c$). However, once the loading is reversed or the specimen is being unloaded (with a finite rate), σ_N is negative (until the specimen is completely unloaded) but $\dot{\sigma}_N$ is now positive giving a negative value of g_N^a and a decrease in the value of g_N^a . This implies that once a specimen is completely unloaded, the residual slip system strength, g_N^a , only stores the contributions from the classical slip system strengthening, g_N^a , due to the accumulated Taylor cumulative shear strain. Moreover, since the value of g_N^a is non-zero only if σ_N is negative, our model predicts that the onset of crystallographic slip under tension will occur when the resolved shear stress on a slip system equals τ_0 , which is the 'intrinsic' critical resolved shear stress of the material, as shown in Fig. 11. In other words, the 'apparent' value of the critical resolved shear stress, τ_{CRSS} , extracted from the crystallographic orientation dependent macroscopic yield strength, σ_N , of the material will be independent of the tensile stress normal to the basal plane, σ_N .

The results of our parametric studies aimed at quantifying the role of the non-Schmid slip resistance on the stress-strain response of the MAX phases revealed that the effects of the non-Schmid component strongly depend on the crystallographic orientation of the micropillars. So that depending on the crystallographic orientation of the micropillars, neglecting the non-Schmid component either has a negligible effect on the stress-strain response or it results in significantly lower initial yield stress as well as flow stress. The effect of limiting the extent of non-Schmid resistance on the stress-strain response of the MAX phases was also found to strongly depend on the crystallographic orientation of the micropillars. That is depending on the crystallographic orientation of the micropillars, not limiting the extent of non-Schmid resistance either has a negligible effect on the stress-strain response or it significantly overestimates the flow stress. Moreover, our results show that the effect of the non-Schmid resistance on the stress-strain response of the micropillars is greater for the Ti₂AlC MAX phase compared to the Ti₃AlC₂ MAX phase.

We also carried out parametric studies to analyze the effects of two key experimental parameters – friction between the rigid punch and top surface of the micropillar, and the vertical taper of the micropillars. Our results show that the effect of the friction between the punch and the micropillars strongly depends on the crystallographic orientation of the micropillars i.e., depending on the crystallographic orientation of the micropillars, an increase in the friction either significantly overestimates the flow stress or has a negligible effect. On the other hand, the presence of a small taper ($<5^{\circ}$) in the MAX phase micropillars of large diameter ($\approx10\mu m$) is found to only slightly affect the initial yield strength, in line with the results obtained from discrete dislocation dynamics simulations of compression of tapered micropillars by Kondori et al. (2017). However, the presence of a small taper in the micropillars increases the flow stress.

Numerous experimental studies on polycrystalline aggregates of MAX phases have highlighted the strong influence of the microstructural features such as grain morphology and texture on their mechanical response. In particular, it has been shown that textured polycrystalline MAX phases at room temperature can exhibit very ductile response under compression with strain to failure exceeding 10% (Barsoum and El-Raghy, 1999). The non-Schmid crystal plasticity constitutive relation formulated in this work can now be used to simulate the mechanical response of polycrystalline aggregate of MAX phases and optimize the microstructural parameters to further enhance their mechanical performance.

5. Conclusion

Motivated by the experimental observations of non-Schmid crystallographic slip in MAX phases, herein, we have formulated a non-Schmid crystal plasticity constitutive relation to predict the single crystal level stress – strain response of two MAX phases, Ti₂AlC and

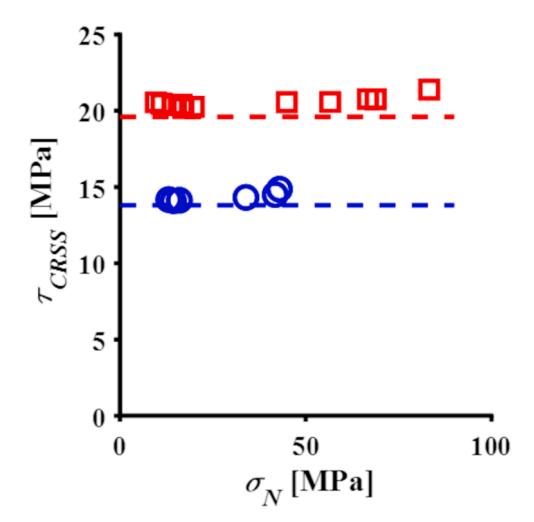


Fig. 11. The variation of the predicted 'apparent' critical resolved shear stress, τ_{CRSS} , with the component of stress normal to the basal plane, σ_N , for Ti₂AlC (open circles) and Ti₃AlC₂ (open squares) MAX phase specimens subjected to uniaxial tensile loading conditions. The corresponding values of the 'intrinsic' critical resolved shear stress, τ_0 , obtained from micropillar compression tests by Zhan et al. (2020, 2021) for the two MAX phases are also plotted as dashed lines.

Ti₃AlC₂. The proposed constitutive relation assumes that the evolution of slip system strength/resistance in MAX phases has two components – a classical component that depends on the Taylor cumulative shear strain and a non-Schmid component that depends on the stress normal to the slip plane. The non-Schmid crystal plasticity constitutive relation is then used to carry out finite element simulations of micropillar compression of the two materials. The finite element simulations not only quantitatively predict the stress – strain response of a wide range of crystallographic orientations of the micropillars but also rationalize the non-uniform deformation and the deformed shape of the micropillars observed in the experiments for the two materials. Parametric studies are also carried out to quantify the role of the non-Schmid slip system resistance and understand the effects of key experimental parameters on the stress – strain response of the micropillars of the two MAX phases. The key conclusions of our work are as follows:

- The effect of the non-Schmid slip system resistance strongly depends on the crystallographic orientation of the micropillars i.e., depending on the crystallographic orientation of the micropillars, neglecting the non-Schmid resistance either has a negligible effect or it predicts significantly lower initial yield and flow stress.
- The contribution of the non-Schmid slip system resistance due to the stress normal to the slip planes in MAX phases saturates once the stress normal to the slip planes reaches a critical value.
- The effect of saturation in non-Schmid resistance to slip strongly depends on the crystallographic orientation of the micropillars i.e., depending on the crystallographic orientation of the micropillars, not limiting the extent of non-Schmid resistance either has a negligible effect or it significantly overestimates the flow stress.
- The effect of the non-Schmid resistance on the stress-strain response of the micropillars is shown to be greater for the Ti₂AlC MAX phase compared to the Ti₃AlC₂ MAX phase.
- The effect of the friction between the punch and the micropillars strongly depends on the crystallographic orientation of the micropillars i.e., depending on the crystallographic orientation of the micropillars, an increase in the friction either significantly overestimates the flow stress or has a negligible effect.
- The presence of a small taper in the MAX phase micropillars of large diameter is found to only slightly affect the initial yield strength.

CRediT authorship contribution statement

Umair Bin Asim: Formal analysis, Investigation, Methodology, Software, Validation, Visualization, Writing – original draft. **Zhiqiang Zhan:** Formal analysis, Investigation, Validation, Visualization, Writing – review & editing. **Miladin Radovic:** Conceptualization, Funding acquisition, Project administration, Resources, Supervision, Validation, Writing – review & editing. **Ankit Srivastava:** Conceptualization, Data curation, Funding acquisition, Methodology, Project administration, Resources, Supervision, Validation, Writing – original draft.

Declaration of Competing Interest

None.

The authors declare that they have no known competing financial interests or personal relationships that could have appeared to influence the work reported in this paper.

Acknowledgments

This material is based upon work partially supported by the U.S. Department of Energy, National Nuclear Security Administration under Award No. DE-NA0003857 and U.S. National Science Foundation grant CMMI - 1944496. The finite element simulations reported on were carried out using high performance research computing resources provided by Texas A&M University.

References

Asaro, R.J., Needleman, A., 1985. Overview no. 42 texture development and strain hardening in rate dependent polycrystals. Acta Metall. 33, 923–953. Barsoum, M., Murugaiah, A., Kalidindi, S., Zhen, T., Gogotsi, Y., 2004. Kink bands, nonlinear elasticity and nanoindentations in graphite. Carbon 42, 1435–1445. Barsoum, M.W., 2013. MAX Phases: Properties of Machinable Ternary Carbides and Nitrides. Wiley.

Barsoum, M.W., El-Raghy, T., 1999. Room-temperature, ductile carbides. Metall. Mater. Trans. A 30, 363-369.

Barsoum, M.W., El-Raghy, T., 2001. The MAX phases: unique new carbide and nitride materials: ternary ceramics turn out to be surprisingly soft and machinable, yet also heat-tolerant, strong and lightweight. Am. Sci. 89, 334–343.

Barsoum, M.W., Farber, L., El-Raghy, T., 1999a. Dislocations, kink bands, and room-temperature plasticity of Ti₃SiC₂. Metall. Mater. Trans. A 30, 1727–1738. Barsoum, M.W., Farber, L., Levin, I., Procopio, A., El-Raghy, T., Berner, A., 1999b. High-resolution transmission electron microscopy of Ti₄AlN₃, or Ti₃Al₂N₂ revisited. J. Am. Ceram. Soc. 82, 2545–2547.

Barsoum, M.W., Radovic, M., 2011. Elastic and mechanical properties of the MAX phases. Annu. Rev. Mater. Res. 41, 195-227.

Bhattacharya, R., Benitez, R., Radovic, M., Goulbourne, N.C., 2014. High strain-rate response and deformation mechanisms in polycrystalline Ti₂AlC. Mater. Sci. Eng. A 598, 319–326.

Brüsewitz, C., Knorr, I., Hofsäss, H., Barsoum, M.W., Volkert, C.A., 2013. Single crystal pillar microcompression tests of the MAX phases Ti₂InC and Ti₄AlN₃. Scr. Mater. 69, 303–306.

Cereceda, D., Diehl, M., Roters, F., Raabe, D., Perlado, J.M., Marian, J., 2016. Unraveling the temperature dependence of the yield strength in single-crystal tungsten using atomistically-informed crystal plasticity calculations. Int. J. Plast. 78, 242–265.

Chen, P., Ghassemi-Armaki, H., Kumar, S., Bower, A., Bhat, S., Sadagopan, S., 2014. Microscale-calibrated modeling of the deformation response of dual-phase steels. Acta Mater. 65, 133–149.

Du, Y.L., Sun, Z.M., Hashimoto, H., Barsoum, M.W., 2009. Theoretical investigations on the elastic and thermodynamic properties of Ti₂AlC_{0.5}N_{0.5} solid solution. Phys. Lett. Sect. A Gen. At. Solid State Phys. 374, 78–82.

Duesbery, M.a.-S., Vitek, V., 1998. Plastic anisotropy in bcc transition metals. Acta Mater. 46, 1481-1492.

Farber, L., 1999. Transmission electron microscopy study of a low-angle boundary in plastically deformed Ti₃SiC₂. Philos. Mag. Lett. 79, 163–170.

Farber, L., Barsoum, M.W., Zavaliangos, A., El-Raghy, T., Levin, I., 1998. Dislocations and stacking faults in Ti₃SiC₂. J. Am. Ceram. Soc. 81, 1677–1681.

Ghorbanpour, S., Alam, M.E., Ferreri, N.C., Kumar, A., McWilliams, B.A., Vogel, S.C., Bicknell, J., Beyerlein, I.J., Knezevic, M., 2020. Experimental characterization and crystal plasticity modeling of anisotropy, tension-compression asymmetry, and texture evolution of additively manufactured Inconel 718 at room and elevated temperatures. Int. J. Plast. 125, 63–79.

Ghorbanpour, S., Zecevic, M., Kumar, A., Jahedi, M., Bicknell, J., Jorgensen, L., Beyerlein, I.J., Knezevic, M., 2017. A crystal plasticity model incorporating the effects of precipitates in superalloys: application to tensile, compressive, and cyclic deformation of Inconel 718. Int. J. Plast. 99, 162–185.

Gouriet, K., Carrez, P., Cordier, P., Guitton, A., Joulain, A., Thilly, L., Tromas, C., 2015. Dislocation modelling in Ti₂AlN MAX phase based on the Peierls–Nabarro model. Philos. Mag. 95, 2539–2552.

Griggs, J., Lang, A.C., Gruber, J., Tucker, G.J., Taheri, M.L., Barsoum, M.W., 2017. Spherical nanoindentation, modeling and transmission electron microscopy evidence for ripplocations in Ti₃SiC₂. Acta Mater. 131, 141–155.

Gröger, R., 2021. Symmetry-adapted single crystal yield criterion for non-Schmid materials. Int. J. Plast. 146, 103101.

Gröger, R., Bailey, A.G., Vitek, V., 2008a. Multiscale modeling of plastic deformation of molybdenum and tungsten: I. Atomistic studies of the core structure and glide of 1/2(1 1 1) screw dislocations at 0 K. Acta Mater. 56, 5401–5411.

Gröger, R., Racherla, V., Bassani, J.L., Vitek, V., 2008b. Multiscale modeling of plastic deformation of molybdenum and tungsten: II. Yield criterion for single crystals based on atomistic studies of glide of 1 /2 \langle 111 \rangle screw dislocations. Acta Mater. 56, 5412–5425.

Gröger, R., Vitek, V., 2020. Single crystal yield criterion for chromium based on atomistic studies of isolated 1/2[111]screw dislocations. Int. J. Plast. 132, 102733. Guitton, A., Joulain, A., Thilly, L., Tromas, C., 2012. Dislocation analysis of Ti₂AlN deformed at room temperature under confining pressure. Philos. Mag. 92, 4536–4546.

Higashi, M., Momono, S., Kishida, K., Okamoto, N.L., Inui, H., 2018. Anisotropic plastic deformation of single crystals of the MAX phase compound Ti₃SiC₂ investigated by micropillar compression. Acta Mater. 161, 161–170.

Huang, Y., 1991. A User-Material Subroutine Incorporating Single Crystal Plasticity in the ABAQUS Finite Element Program, Mech report 178. Harvard Univ., pp. 1–3 Knezevic, M., Beyerlein, I.J., Lovato, M.L., Tomé, C.N., Richards, A.W., McCabe, R.J., 2014. A strain-rate and temperature dependent constitutive model for BCC metals incorporating non-Schmid effects: application to tantalum–tungsten alloys. Int. J. Plast. 62, 93–104.

Koester, A., Ma, A., Hartmaier, A., 2012. Atomistically informed crystal plasticity model for body-centered cubic iron. Acta Mater. 60, 3894–3901.

Kondori, B., Needleman, A., Benzerga, A.A., 2017. Discrete dislocation simulations of compression of tapered micropillars. J. Mech. Phys. Solids 101, 223–234. Kooi, B.J., Poppen, R.J., Carvalho, N.J.M., De Hosson, J.T.M., Barsoum, M.W., 2003. Ti₃SiC₂: a damage tolerant ceramic studied with nano-indentations and transmission electron microscopy. Acta Mater. 51, 2859–2872.

Lagarias, J.C., Reeds, J.A., Wright, M.H., Wright, P.E., 1998. Convergence properties of the Nelder–Mead simplex method in low dimensions. SIAM Journal on optimization 9, 112–147.

Lane, N.J., Vogel, S.C., Caspi, E.N., Barsoum, M.W., 2013. High-temperature neutron diffraction and first-principles study of temperature-dependent crystal structures and atomic vibrations in Ti_3AlC_2 , Ti_2AlC , and $Ti_5Al_2C_3$. J. Appl. Phys. 113, 183519.

Lim, H., Hale, L.M., Zimmerman, J.A., Battaile, C.C., Weinberger, C.R., 2015. A multi-scale model of dislocation plasticity in α -Fe: Incorporating temperature, strain rate and non-Schmid effects. Int. J. Plast. 73, 100–118.

Mapar, A., Ghassemi-Armaki, H., Pourboghrat, F., Kumar, K.S., 2017. A differential-exponential hardening law for non-Schmid crystal plasticity finite element modeling of ferrite single crystals. Int. J. Plast. 91, 268–299.

Molina-Aldareguia, J.M., Emmerlich, J., Palmquist, J.P., Jansson, U., Hultman, L., 2003. Kink formation around indents in laminated Ti₃SiC₂ thin films studied in the nanoscale. Scr. Mater. 49, 155–160.

Patra, A., Zhu, T., McDowell, D.L., 2014. Constitutive equations for modeling non-Schmid effects in single crystal bcc-Fe at low and ambient temperatures. Int. J. Plast. 59, 1–14.

Peirce, D., Asaro, R.J., Needleman, A., 1982. An analysis of nonuniform and localized deformation in ductile single crystals. Acta Metall. 30, 1087-1119.

Plummer, G., Barsoum, M.W., Weinberger, C.R., Tucker, G.J., 2022. Basal dislocations in MAX phases: core structure and mobility. Materialia 21, 101310. Qin, Q., Bassani, J.L., 1992. Non-schmid yield behavior in single crystals. J. Mech. Phys. Solids 40, 813–833.

Radovic, M., Barsoum, M.W., 2013. MAX phases: bridging the gap between metals and ceramics. Am. Ceram. Soc. Bull. 92, 20-27.

Smith, J.F., Vishnyakov, V.M., Davies, M.I., Beake, B.D., 2013. Nanoscale friction measurements up to 750 °C. Tribol. Lett. 49, 455–463.

Sokol, M., Natu, V., Kota, S., Barsoum, M.W., 2019. On the Chemical Diversity of the MAX Phases, Trends in Chemistry. Cell Press, pp. 210–223.

Srivastava, A., Ghassemi-Armaki, H., Sung, H., Chen, P., Kumar, S., Bower, A.F., 2015. Micromechanics of plastic deformation and phase transformation in a three-phase TRIP-assisted advanced high strength steel: experiments and modeling. J. Mech. Phys. Solids 78, 46–69.

- Tan, J., Han, H., Wickramaratne, D., Liu, W., Zhao, M., Huai, P., 2014. A comparative first-principles study of the electronic, mechanical, defect and acoustic properties of Ti_2AIC and Ti_3AIC . J. Phys. D Appl. Phys. 47, 8.
- Tromas, C., Villechaise, P., Gauthier-Brunet, V., Dubois, S., 2011. Slip line analysis around nanoindentation imprints in Ti₃SnC₂: a new insight into plasticity of MAX-phase materials. Philos. Mag. 91, 1265–1275.
- Wang, J., Zhou, Y., 2004. Dependence of elastic stiffness on electronic band structure of nanolaminate M₂AlC (M=Ti,V,Nb, and Cr) ceramics. Phys. Rev. B Condens. Matter Mater. Phys. 69, 214111.
- Weinberger, C.R., Battaile, C.C., Buchheit, T.E., Holm, E.A., 2012. Incorporating atomistic data of lattice friction into BCC crystal plasticity models. Int. J. Plast. 37, 16–30
- Xiao, J., Yang, T., Wang, C., Xue, J., Wang, Y., 2015. Investigations on radiation tolerance of $M_{n+1}AX_n$ Phases: Study of Ti_3SiC_2 , Ti_3AlC_2 , Cr_2AlC , Cr_2GeC , Ti_2AlC , and Ti_2AlN . J. Am. Ceram. Soc. 98, 1323–1331.
- Zhan, Z., Chen, Y., Radovic, M., Srivastava, A., 2020. Non-classical crystallographic slip in a ternary carbide Ti₂AlC. Mater. Res. Lett. 8, 275-281.
- Zhan, Z., Radovic, M., Srivastava, A., 2021. On the non-classical crystallographic slip in Ti_{n+1}AlC_n MAX phases. Scr. Mater. 194, 113698.
- ABAQUS/Standard, User's Mannual, 2020. Dassault Systemes, Vélizy-Villacoublay, France.